Chapter 5

Successive VO_2 Phase Orders at Frequency Induced $3d^1$ Electrons Order of Metallizing Surface States in Thin VO_2@SiO_2-Si films

5.1 Introduction

The utilities for VO_2 at RT need to tune critical point (T_c ~ 340 K) in a wide band, usually 315 ± 25 K [1, 2], of a tunable SMT signal of the exotic properties. Among all, lattice strain and metallic doping (or O^{2-} vacancies) are two common recipes to suppress T_c and extend SMT in a specific range of deep metallic VO_2 states [1, 3]. Adversely, unless duly optimized, the localized defects hinder the useful properties [1, 3].

Extensive studies on VO_2 in different forms over decades, its technology has motivated to integrate in multiple devices mainly in the last few years. The basic stimuli are chemical strain [4, 5], epitaxial strain [6, 7], electrochemical modulation [8, 9], photoexcitation [2, 10], hydrogenation [11, 12], and electric field effects [4, 13, 14]. In general, a hole 'h^+' creates (promotes VO_2 metallicity) in the valence band (VB) at an electron 'e^-' excites from the conduction band (CB), across the bandgap (E_g) = 0.7 eV [15, 16], as mobile 'e^--h^+' pairs. Coupled 'e-p' order near the E_F filling up the E_g towards the metallic VO_2 states. How the stimuli induce and control over the charge order of emerging properties is an open issue [7–9, 15]. Epitaxial films VO_2 (at limited thickness $t \leq 100$ nm) [13, 16], embedding unified VO_2 NCs in small islands (clusters) are a model system to explore such issues and their impacts on the technologies.

A nanophase can undergo a local surface order in a 1 → 2D structure [7, 17]. Successive phases emerge one over others if they order duly slowly in steps at a time scale. Thus, the mixed states order and coexist to support one over others in order of their competing stabilities. The net VO_2 gets metallized at their electric fields (as electrolyte gates) [14, 18] at rather low temperatures.

In this chapter, we report the $M_1 \rightarrow M_2/R_1/R_2/R\text{-}VO_2$ phases can be discriminated at order successively at radio frequencies (RFs), which mobilize the exotic charges in the impedance resistance (Z) declines (up to 10^5 times) and conductivity (σ_{ac}) rises up in due steps at a measurable scale. Thus, near 10^6 Hz, the R-VO_2 orders even at RT. It is a model example of a VO_2 phase order at no phase separation [17]. The studies are done at thin films (011) VO_2@SiO_2-Si at 303 K to 473 K temperatures across the T_c point to insight the role of kinetically decoupled 'e-p' on the charge order. Here, the RF induces, regulates, and monitors charge order at modulated 'e-p' interactions at the SC → R-VO_2 states. They are mapped in-situ at an optical response of the s-SNOM images [19–22]. The results are described in correlation to XRD, AFM, TEM, and lattice images of the M_1-VO_2 films. A large strain is shown in anharmonic (011) and (022) lattices. It relaxes in a surface charge order. A density DFT is applied to express the VO_2 phase order.

5.2 Results and Discussion

5.2.1 Thin Films VO_2@SiO_2-Si of Strained$_{011}$/d_{022} Layers

The thin VO_2 films (t ~ 60 nm) spin-coated at a (100) Si(p^{++}) substrate via a nanogate SiO_2 (t ~ 10 nm) are well ordered in d_{011} and d_{022} layers (NCs) along the film surface. As a result, a typical XRD pattern of the films (annealed 3 h at 823 K in Ar gas) in **Figure 5.1 (a)** exhibits only two peaks of M_1-VO_2 of d_{011} = 0.3254 nm and d_{022} = 0.1611 nm at

$2\theta = 27.39°$ and 57.13°, respectively. Both d_{011}/d_{022} layers are strictly tied up along the M_1-VO_2 *a*-axis of no any other peak is visible in this region. Both peaks are single and symmetric shaped as illustrated in a magnified d_{011} view in the inset in **Figure 5.1 (a)**. A broad $d_{300} = 0.1362$ nm peak ($d_{300}^* = 0.1400$ nm bulk value) [17] is shown in the (100) SiO_2 at 68.90° in a compressive strain (γ_c) = $(d_{300} - d_{300}^*)/d_{300}^* \cong (-)$ 2.71%, is built up in the VO_2 is bonding via 'Si-O' bonds along its *a*-axis of anisotropic network. A similar $\gamma_c = (-)$ 3.00 % prevails in the nanogate SiO_2@Si of a major XRD peak is shown at $d_{300} = 0.1358$ nm in the inset in **Figure 5.1 (a)**. Further, an intensity ratio $I_{022}/I_{011} = 9.0$ % is reduced in the d_{011}/d_{022} M_1-VO_2 peaks ($I_{022}/I_{011} = 14.3\%$ at bulk sample) [23] in the d_{011}/d_{022} layers M_1-VO_2 are aligned facing up at the films (shown in the inset). Their peak widths (β) give $\gamma_c = 0.31\%$ at a $D_e \sim 25$ nm in the Williamson-Hall relation [24], $\beta\cos\theta = k\lambda/D_e + \gamma_c\sin\theta$, at a correlation $k = 0.9$ factor [16, 24]. As shown in **Figure 5.1 (b)**, an anharmonicity $\delta = d_{022} - \frac{1}{2}d_{011} = (-)$ 0.0026 nm gives $\gamma_c = 2\delta/d_{011} \cong (-)$ 1.60% in the d_{022} is stained at the d_{011} layers. Otherwise, $\gamma_c \sim 0$ at $d_{011} = 0.32034$ nm and $d_{022} = 0.16017$ nm ($\delta \sim 0$) in the bulk M_1-VO_2 crystals [17]. **Figure 5.1 (c)** projects a way a d_{011} layer in a M_1-VO_2 lattice ($z = 4VO_2$) turns up in an R-VO_2 lattice ($z = 2VO_2$). Unless twines (strains further), a strained M_1-VO_2 releases its strain to order towards relatively lower energy R-VO_2 states [25, 26].

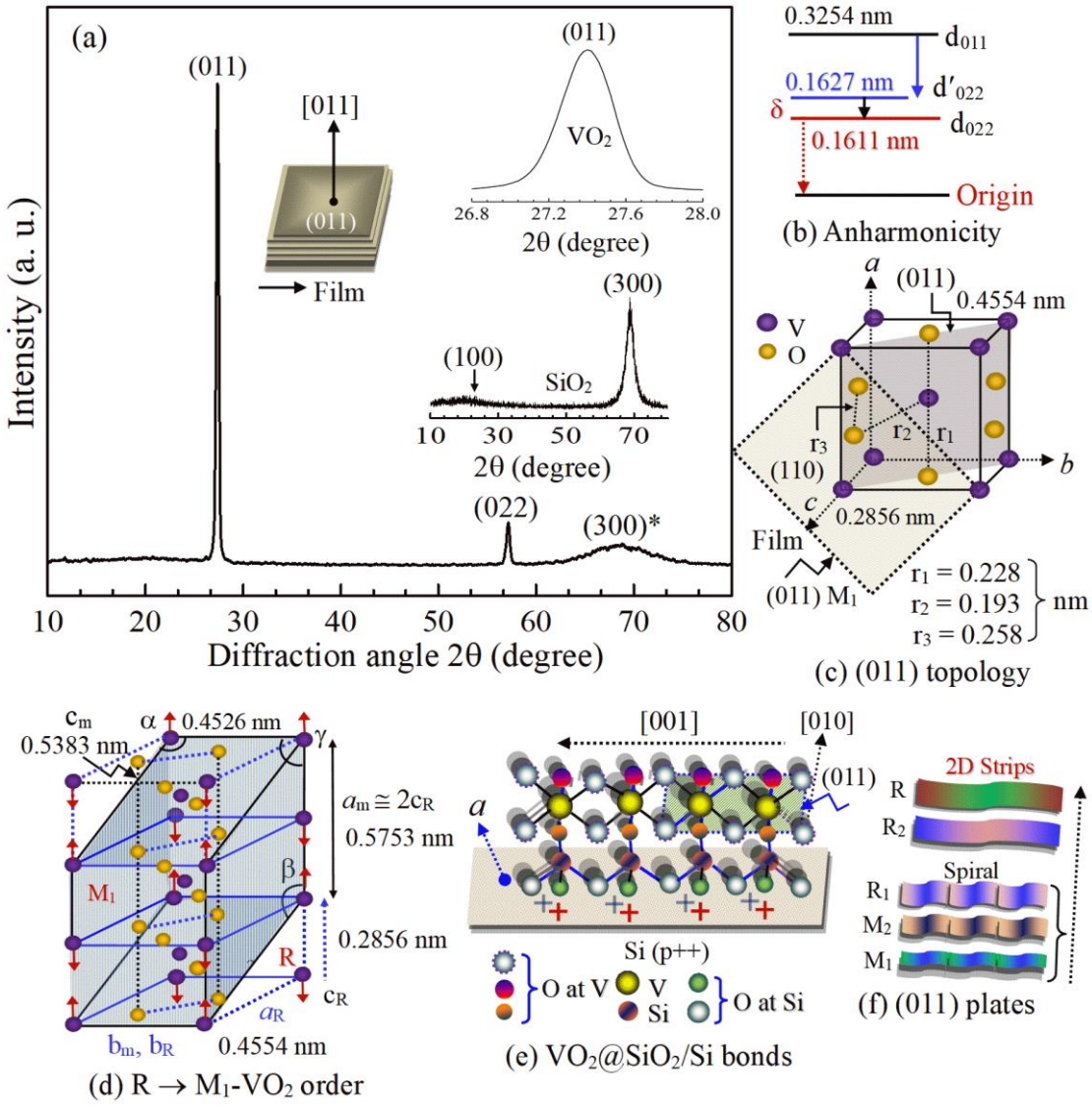

Figure 5.1 (a) XRD pattern of (011) uniaxial M_1-VO_2 grown at Si (p^{++}) via a SiO_2 nanogate (of XRD in the inset). The (011) peak zoomed in the inset shows its symmetric shape. *The SiO_2 peak. (b) A compressive d_{022} strain, (c) an R-VO_2 lattice order at a coherent (011) M_1-VO_2 facet along the film, (d) a strain induced R ↔ M_1-VO_2 order, (e) a charge-induced VO_2 bonding @SiO_2/Si surface, and (f) an M_1-VO_2 surface order (on heating) leading to the SC → metallic VO_2 states at $3d^1$-V^{4+} delocalized electrons at the planar 2D nanostrips.

The d_{011} M_1-VO_2 plane swipes into d_{110R} plane in the M_1-VO_2 *a*-axis (a_m) is exchanged with the R-VO_2 c-axis (c_R) of $a_m \cong 2c_R$ at z = 4VO_2 per unit cell. It is a strain-induced surface order. Thermodynamically, a M_1-VO_2 lattice orders towards higher symmetry VO_2 phases. An octagon R-VO_6^{8-} involves r_1 = 0.228 nm (V^{4+}-O^{2-} distance) along a_R,

while r_2 = 0.193 nm on the d_{011} plane, with r_3 = 0.258 nm (O^{2-}-O^{2-} distance) [27]. Uneven V^{4+}-O^{2-} bonds along the three axes result in the lower symmetry VO_2 phases. **Figure 5.1 (d)** elucidates a schematic of a surface R-VO_2 → M_1-VO_2 order; an upgraded view from the work of Wentzcovitch [28]. The arrows mark the M_1-VO_2 distorts at V^{4+} displaces along a_m at it rises to $2c_R$ and β = 90° rises to 122.6° [23]. At a small energy, ≤ 30 meV per atom, an ab initio calculation displays four more monoclinic VO_2 phases; two almost degenerate, one ferromagnetic (FM) and other antiferromagnetic (AFM), which arise at 15 GPa pressure.

As shown in **Figure 5.1 (e)**, a nanogate SiO_2@(100)Si(p^{++}) bonds over VO_2 via O^{2-} of a negatively charged network layer of a 2D interface. It acts as an electrolyte a way to it controls, directs, and monitors the VO_2 order along the local charge fields. Thus, a perpetual M_1-VO_2 structure grows up in d_{011}/d_{022} chains at the V^{4+}-O^{2-}-SiO_2/Si bonds. It lies along its c_m at a_m facing up at the interface at an angle β. The V^{4+} bonding to SiO_2 via O^{2-} along a_m results in a (011) M_1-VO_2 lattice growing up as long as it follows the local fields. As a matter of fact, the 'a_m' is taken facing up at the interface in accords to XRD in the VO_2 films. In this scheme, the VO_2 keeps on order united primarily along the V^{4+}-O^{2-}-Si^{4+} bonds in a single non-disrupted process. Thus, a uniaxial d_{011}/d_{022} VO_2 pattern lasts at a nanoscale in a specific shape (nanoplates, nanobeams, or nanoprisms) in the strictly controlled conditions. More complex M_1-VO_2 shapes can emerge in multiple growth topologies. A surface order M_1-VO_2 → M_2/R_1/R_2/R-VO_2 is paved at no phase separation, as projected in **Figure 5.1 (f)**, where the zigzag M_1-VO_2 chains (spirals) are gradually turned down in planar R-VO_2 stripes at deep surface order. The TEM images in **Figure 5.2 (a, b)** reveal two major types M_1-VO_2 architects (i) pentagonal nanoprisms

(or nanobeams), with height h = 20-30 nm at w = 30-60 nm widths, and (ii) nanoplates of a layer structure (w ~ 45 nm and t ~ 8 nm) in a bimodal pattern.

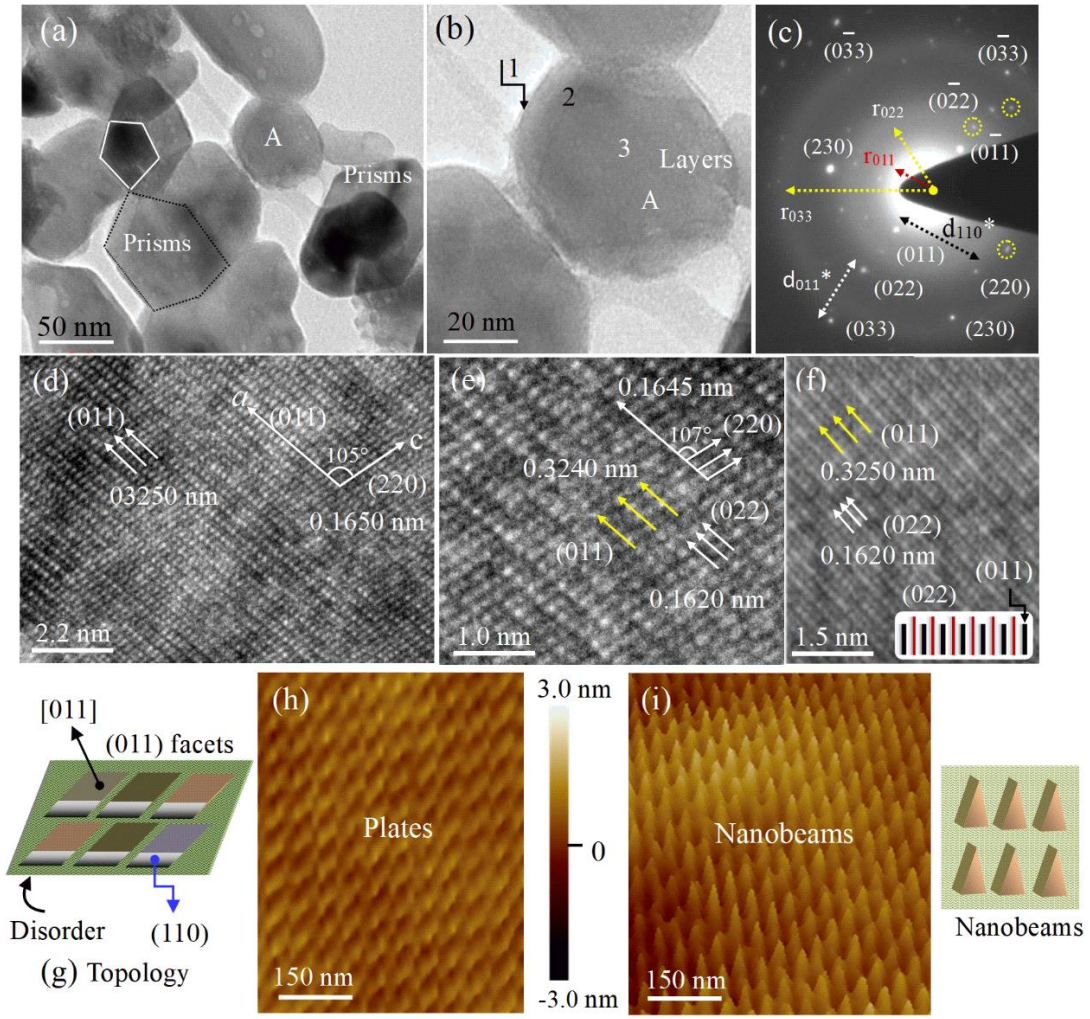

Figure 5.2 HRTEM images of (a) distorted polytopes and (b) thin layers (plates), (c) SAED pattern (plate A) of $d_{011} = d_{011} \cong 0.3250$ nm, $d_{022} \cong 0.1620$ nm and $d_{033} \cong 0.1050$ nm arrays of spots superposed on diffused rings of radii $r_{011} = (0.3730 \text{ nm})^{-1}$, $r_{022} = (0.1860 \text{ nm})^{-1}$ and $r_{033} = (0.1210 \text{ nm})^{-1}$ of a disorder VO_2, (d, e, f) lattices from different parts at plate A, (g) a model two-phase structure, and (h, i) 2D/3D AFM images from the VO_2@SiO_2-Si films. Twins in (c) are marked at the circles.

Three layers 1, 2, 3 are marked led one over others in a plate 'A' in **Figure 5.2 (b)**. A SAED taken at this region in **Figure 5.2 (c)** contains $(d_{011})^{-1}$, $(d_{022})^{-1}$, and $(d_{033})^{-1}$ arrays

of sharp spots (at a separation $d_{011}^{*} = (d_{011})^{-1} \cong 0.3250$ nm) along with three diffuse rings of radii $r_{011} = (0.3730\ nm)^{-1}$, $r_{022} = (0.1860\ nm)^{-1}$ and $r_{033} = (0.1210\ nm)^{-1}$ in a reciprocal lattice scale. The rings display 15% lager d_{011}, d_{022} and d_{033} of a disordered (softer) M_1-VO_2 (φ_2) in a surface order on the NCs (φ_1). Further, a few spots (marked at the circles) are displaced off the regular arrays in the M_1-VO_2 is twined at the $\varphi_1 - \varphi_2$ interfaces [16, 29]. The small φ_2 part (a roughly under 10 %) is not visible in the XRD in the corresponding peaks (weak) are masked in the prominent S_1 peaks. A site mismatch creates twin at irregular sites, deviation from a V^{4+} charge state, local disorder, vacancies, or competing $\varphi_1 - \varphi_2$ orders [16, 29]. We also studied the lattice structures in terms of the lattice images. For example, **Figure 5.2 (d, e, f)** corroborate the results, in which the plate 'A' in **Figure 5.2 (b)** contains d_{011}, d_{220} and d_{033} lattice arrays shown in the SAED in **Figure 5.2 (c)**. In **Figure 5.2 (d)**, $d_{011} = 0.3250$ nm and $d_{220} = 0.1650$ nm patterns intersect at $\beta = 105.0°$, a reduced value from 122.6° in M_1-VO_2 [23]. $\beta = 107.0°$ is observed at similar diffused strips (strained) at $d_{011} = 0.3240$ nm and $d_{220} = 0.1645$ nm in **Figure 5.2 (e)**. It refers to M_2-VO_2 [30] is ordered in thin layers of larger enthalpy [25, 26], at RT. Sharp strips $d_{011} = 0.3250$ nm and $d_{022} = 0.1620$ nm shown in **Figure 5.2 (f)**, with a stick pattern at the bottom, arise in the M_1-VO_2 is relaxed. **Figure 5.2 (g)** describes a simple model of VO_2 NCs are buried in a disordered bed in thin VO_2@SiO_2-Si films. The $d_{011}$and d_{220} values in a crystallography relation [16],

$$\frac{1}{d_{hkl}^2} = \frac{h^2}{a^2 sin^2\beta} + \frac{k^2}{b^2} + \frac{l^2}{c^2 sin^2\beta} - \frac{2hl\ cos\beta}{ca \cdot sin^2\beta} \quad (1)$$

provide working relations

$$\frac{1}{a^2} = \frac{1}{c^2} + \left[\left(\frac{1}{2d_{220}}\right)^2 - \left(\frac{1}{d_{011}}\right)^2\right] sin^2\beta \quad (2)$$

$$\frac{1}{b^2} = \frac{1}{d^2{}_{011}} - \frac{1}{c^2 sin^2 \beta} \quad (3)$$

which give a = 0.5603 nm and b = 0.4164 nm at d_{011} = 0.3250 nm, d_{220} = 0.1650 nm, and β =105.0°, assuming the same c = 0.5383 nm as in a bulk M_1-VO_2 [23]. Thus, a lattice volume (V_c) = abc·sinβ ≅ 0.1213 nm^3 is 2.71% enhanced from the bulk V_c = 0.1181 nm^3 (a = 0.5753 nm, b = 0.4526 nm, c = 0.5383 nm, and β = 122.6°) [17] in duly higher energy M_2-VO_2 states.

The 2D AFM images of the films VO_2@SiO_2-Si in **Figure 5.2 (h)** reveal small plates (*w* ~ 20 nm and *t* ~ 15 nm at *L* ~ 45 nm length) are binding in chains. A 3D view in **Figure 5.2 (a)** insights they are in fact of pyramidal shapes (*w* ~ 20 nm and *L* ~ 45 at *h* ~ 80 nm) of models given in a right panel. The NCs (φ_1) bonding via the φ_2 part (a binder) in zigzag chains. Further, in situ mapping of MIR s-SNOM images display a way the VO_2 orders in the films (scanned at 1 μm x 1 μm area) in **Figure 5.3** at elevated temperatures. They are demodulated in an optical signal of scattered light at a tipping frequency, which is studied at third harmonic (S_3) of the tip frequency of MIR (~125 meV) at a normalized scale [19–22]. Thus, at 303 K, a deep bluish colour M_1-VO_2 glows in **Figure 5.3 (panel-1)**, which is diminished at 318 K in a $M_1 \rightarrow M_2$-VO_2 surface order. At 323 K, orange colour stripes M_2-VO_2 are shown up at the M_1-VO_2 expense (bluish) in a kinetic phase order. At 328 K, only a fewer M_1-VO_2 lasts (spheroids, ≤ 20 nm size) at M_2/R_1-VO_2 of modified orange/yellowish colours. At duly enhanced optical conductivity at T_c ~ 343 K [21, 22], a pale yellowish contrast is spread at the entire range of the deep R_2/R-VO_2 M-states. Near the T_c onset, the colour is gradually changed **(Figure 5.3, panel-2)** over enhanced metallicity at decoupled 'e-p' states. The intermediate VO_2 phases are well

discriminated in the MIR images are mapped at near the film surface in **Figure 5.3 (panel-3)**.

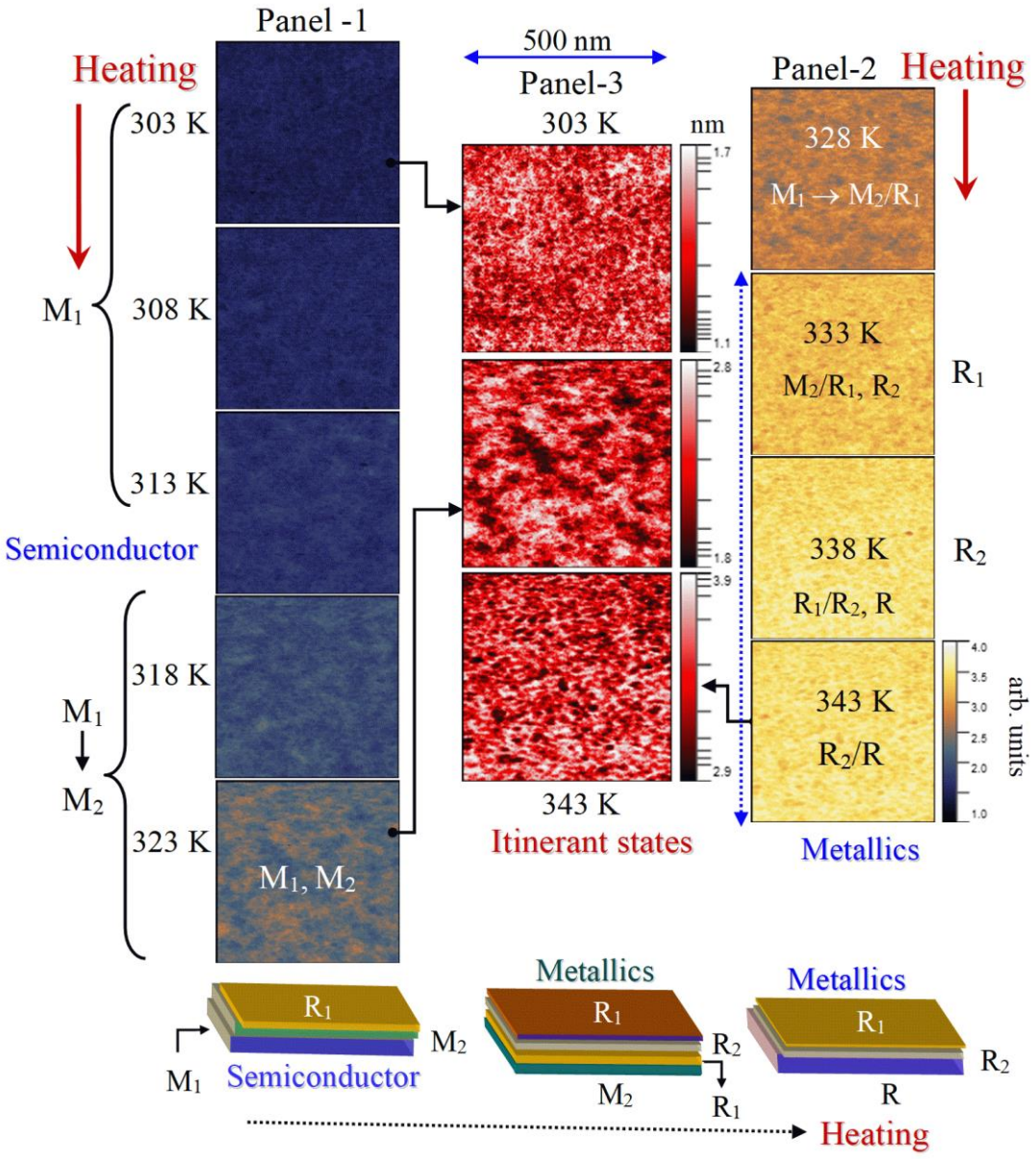

Figure 5.3 The near-field MIR s-SNOM images at surface phase order in a thin M_1-VO_2 film at 303 K → 343 K (panels 1, 2), with a closer view of thermal contrast across the T_c in panel-3. At the bottom, a model projects a competing $M_1 \rightarrow M_2 \rightarrow R_1 \rightarrow R_2$/R-$VO_2$ order.

Thus, at 303 K, small stripes (bluish) of a presumed M_2-VO_2 (~10%) are dispersed in the M_1-VO_2 stripes (reddish), ≤ 25 nm sizes, in strong FM/electrostatic interactions. At 323 K, the M_2-VO_2 is grown up (≤ 50 %) on the M_1-VO_2 of longer chains.

In general, a thermal (or other stimuli) induced surface VO_2 order proceeds in a route of it lowers the net energy [26, 31]. It differs than a phase VO_2 separation in ferroelastic (FE) domains at a substrate, or a nucleation and growth from a bulk VO_2 phase [17, 20]. In this view, at the T_c point, even a less probable phase R_2-VO_2 to exist at such high temperature is shown in **Figure 5.3 (blackish) in panel-3**. It is finely dispersed in the rich phase R-VO_2 (reddish) at a nanoscale. A model at the bottom in **Figure 5.3** displays the VO_2 thus can order and coexist in even otherwise unstable states. A refined VO_2 behaves metallic in its large surface energy. Accordingly, a He^+ injected M_1-VO_2 (refined) shows up MIR R-VO_2 images [22]. The flexible VO_2 chains duly transfer energy in the molecular electronics [16, 32]. The MIR images thus well discriminate even the transient VO_2 orders. Otherwise, MIR images are considered to probe merely the SMT band at no detectable change at the other VO_2 states [21]. The THz (5-10 meV) images are regarded to probe more regular near-field signals of the electronic response at near the E_F surface [21]. In fact, the VO_2 phases clearly differ in the MIR s-SNOM images at near the film surface up to a limited depth (≤ 4 nm). Otherwise, they appear to overlapping one over others difficult to discriminate.

5.2.2 Dynamics of VO_2 Phase Order at Frequencies

The s-SNOM images of VO_2 forestall that frequency is a vital tool to harvest the ‘e-p’ interaction and its impacts on the correlated VO_2 phase order. As a result, the T_c point is duly shifted (at decoupled $3d^1$-VO^{4+} electrons) from 342 K at THz to 350 K at near 10^2 THz (MIR region) [21, 22]. Logically, at temperatures $T \leq T_c$, the frequency induces,

controls, as well as probes (its response) a surface charge order across the E_F surface. Here, the E_g is regularly filled up at the σ_{ac} rises up towards the M-VO_2 states. Exotic 'e^--h^+' charges, induced at $3d^1$-VO^{4+} electrons excite from VB to CB, order at the permeable VO_2 states, which can be tailored at exciting across the E_F surface at a wide range of 10^2 Hz to 10^{15} Hz frequencies. This is illustrated systematically here in terms of σ_{ac} and impedance $Z = Z' + jZ''$, where Z' and Z'' ($j = \sqrt{-1}$) are its real and imaginary parts, respectively. The data are taken at RF frequencies at the VO_2@SiO_2-Si films at selected 303 K to 473 K temperatures at a small step (≤ 10 K) as follows.

Figure 5.4 (a) portrays the σ_{ac} over frequency (f) at a logarithm scale measured at selected temperatures of 303 K to 353 K at the films. It is progressively enhanced in raising both temperature and frequency; up to 40 times at the temperatures, while up to 10^3 times at the 10^2 Hz to 10^6 Hz frequencies. No abrupt σ_{ac} rise is marked at the T_c point in the VO_2 is metallized gradually at the surface order. A continuous change is also shown in the THz s-SNOM images [21]. An abrupt σ_{ac} rise rather appears at 353 K, i.e. well beyond $T_c \sim 343$ K, at $5x10^3$ Hz at point 'P' in a $R_1 \rightarrow R_2$-VO_2 surface order follows the R-VO_2 dominates later at 10^5 Hz. **Figure 5.4 (b)** plots a shallow 'dip' in $\ln\sigma_{ac}$ Vs T at $T_c \sim 343$ K (at 10^2 Hz), which is gradually filled up on a R_1/R_2-VO_2 surface order at later frequencies. It anticipates a charge-induced VO_2 phase order proposed in **Figure 5.3 (bottom)**. At 10^6 Hz, a derivative $\partial\sigma_{ac}/\partial T = \sigma_{ac}^*$ in **Figure 5.4 (c)** shows up a dip at 333 K due to an $M_2 \rightarrow R_1$-VO_2 surface order. Here, the $T_c \sim 343$ K shows up only an inflection that does not shift over the frequencies. A model diagram in **Figure 5.4 (d)** illustrates the RFs (≤ 4.1 neV) induce $3d^1$-V^{4+} electrons that order near the E_F surface, filling up the E_g gap between oppositely charged CB and VB states (as a capacitor). A Joule heating conducts the correlated VO_2 charge/phase orders. Decoupled 'e^--h^+' promote metallicity at modulated

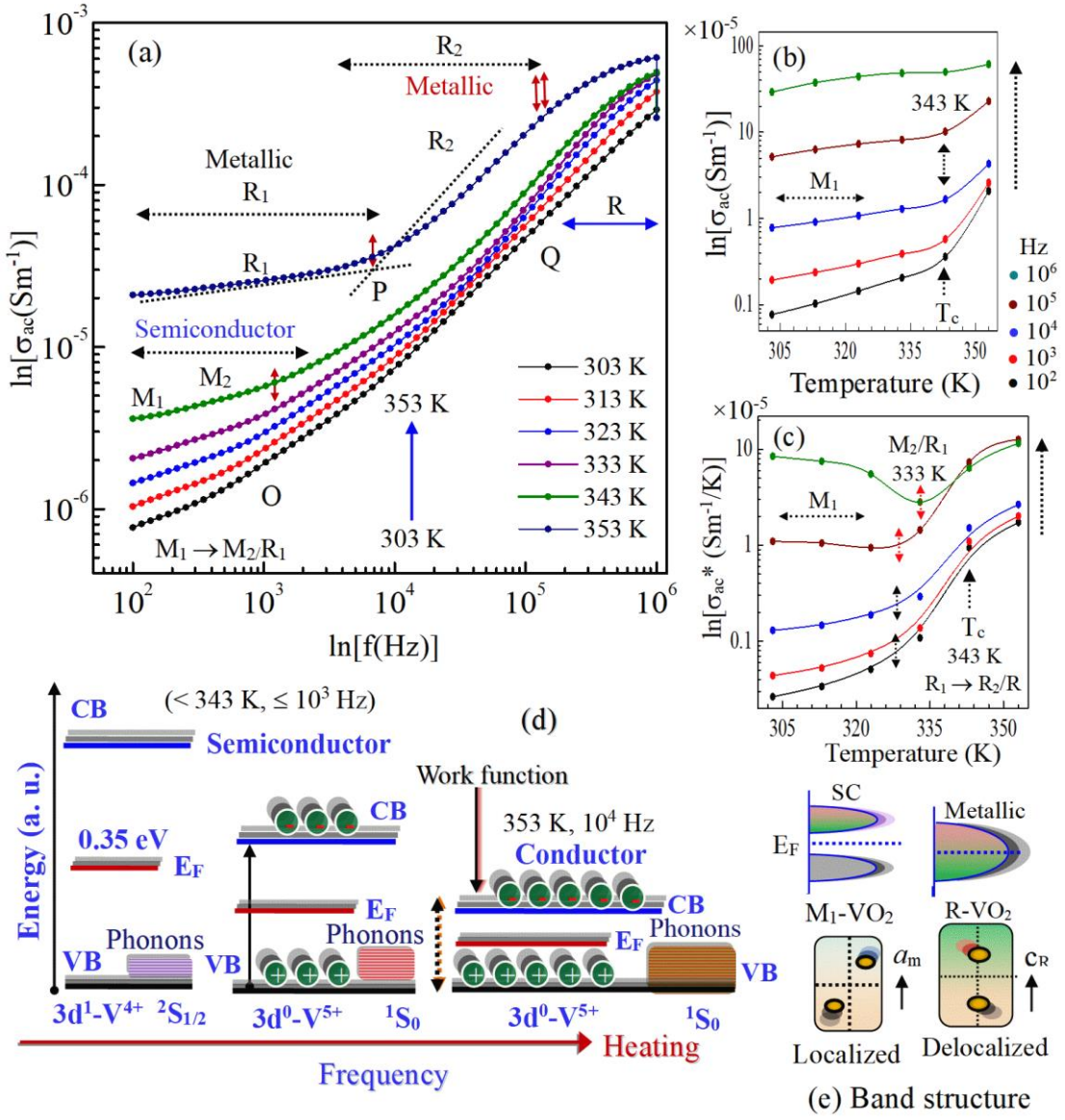

Figure 5.4 (a) The σ_{ac} as a function of frequency (1 Hz to 10^6 Hz) at the thin film VO_2@SiO_2-Si at 303 K to 353 K across the T_c point, (b) temperature dependent σ_{ac} and (c) its derivatives at selected frequencies showing thermal induced $M_1 \rightarrow M_2/R_1/R_2/R$-$VO_2$ orders, and (d, e) model band-energy diagrams at thermal/frequency induced charge orders.

work function at $V^{4+} + h^+ \rightarrow V^{5+}$ mobile charges created in the CB [16, 33]. Thus, even at 300 K, the VO_2 phonons (≤ 125 meV) [34–37] and harmonics have sufficient energy to pump up 'e^-' across the E_g at kT ≅ 25.9 meV (k = Boltzmann constant). **Figure 5.4 (e)**

illustrates a way $3d^1$-V^{4+} orbitals at the M_1-VO_2 states get delocalized along the conductive c_R axis at the R-VO_2 states ($E_g \rightarrow 0$).

Conveniently, the impedance is measured in an out-of-plane parallel plate 'capacitor' geometry in the electric field lines are mostly facing up the film surface [38]. This setup adds up a negligibly small film value in those between the top-top electrodes of a much larger distance. Thus, it gives ultimately an average value in an in-plane setup only [16, 38]. So obtained Z′/Z″ plots (measured at a dc-bias field 1.0 V and 1 mV ac field) at a logarithm scale over 10^2 Hz to 10^6 Hz in **Figure 5.5** display the frequency indorses a surface order $M_1 \rightarrow$ $M_2/R_1/R_2$/R-VO_2 at rather low temperatures. Even at 303 K, both Z′/Z″ fall down progressively, $\leq 10^5$ times, towards the metallized R-VO_2 states of steady values after 10^4 Hz in **Figure 5.5 (a, b)**. At raising temperature, the Z′/Z″ decline gradually up to $T_c \cong 343$ K at the $M_1 \rightarrow M_2$-VO_2 states, while bit faster near 353 K at a R_1/R_2-VO_2 order. The plots bifurcate at the lower frequencies. Prominent 'e-e' interactions render the metallicity at decoupled 'e-p' states. As marked at a zoomed scale in **Figure 5.5 (c, d)**, the electronic (T_{ce}) and structural (T_{cs}) parts are separated apart over the frequencies; T_{cs} follows T_{ce} at a deep charge order. Any M_2-VO_2 if extends beyond T_c ~ 343 K, is metalized exhibiting a strong peak at $5x10^2$ Hz in **Figure 5.5 (d)**, before the $R_2 \rightarrow$ R-VO_2 orders (a weak peak) at 353 K in lieu of a kinetic process. Further, a semi-metallic part R_1/R_2-VO_2, if extends beyond the T_c point, is rapidly metallized at the higher frequencies. **Figure 5.5 (e)** displays the R_1-VO_2 passes via a wide plateau (363 K to 393 K) to order in R_2/R-VO_2 of T_{ce} displaced at 20 kHz. A peak is evolved in a $R_1 \rightarrow R_2$-VO_2 order near 10^4 Hz in **Figure 5.5 (f)** in Z″ as it is highly sensitive to the surface order [39, 40]. A surface-charge keeps R_1/R_2-VO_2 stay till such high temperatures. Now, let us view the Z″ Vs Z′ Nyquist plots at correlated dynamics of the VO_2 charge-phase orders over

303 K to 473 K temperatures and 10^2 to 10^6 Hz frequencies. The data cover a wide range across the T_c point (taken at ≤ 10 K intervals) in order to visualize the closely spaced charge-induced VO_2 orders.

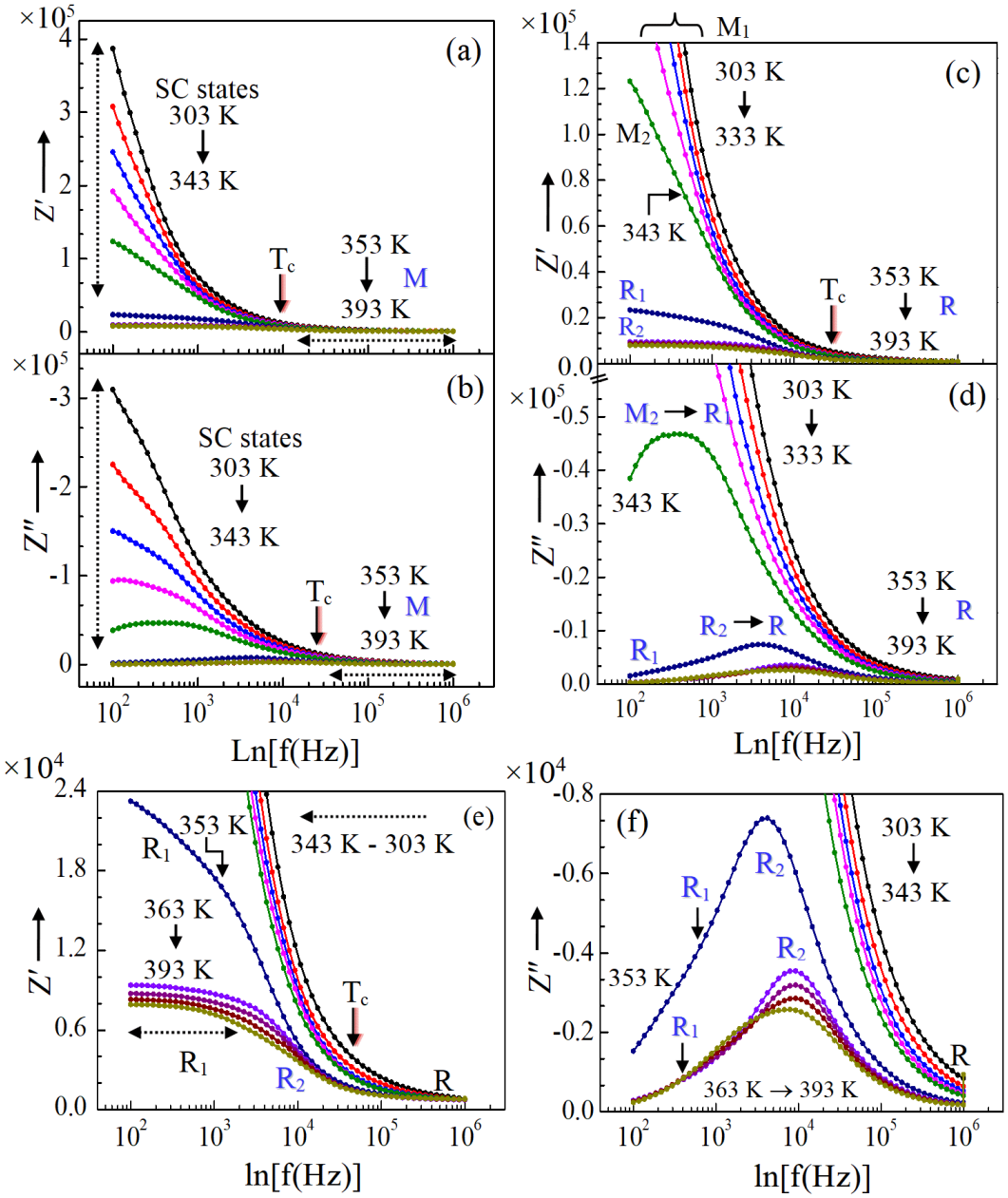

Figure 5.5 The real Z′ (a) and imaginary Z″ (b) parts of impedance resistance, which are zoomed in (c, d) respectively, showing frequency-induced partial $M_1 \rightarrow M_2 \rightarrow R_1/R_2/R\text{-}VO_2$ orders at the films $VO_2@SiO_2$-Si at temperature is raised in steps of 10 K over 303 K to 393 K. (e, f) Decreased Z′ and Z″ at dominant R_1, R_2, R-VO_2 states.

At raising temperature, ≤ 333 K, a parabolic Z′′ Vs Z′ trajectory in **Figure 5.6 (a)** is gradually converged towards a semicircle (metallization) at the $M_1 \rightarrow M_2$-VO_2 orders. At $T_c \sim 343$ K, two mini semicircles are overlapping each other at the R_1/R_2-VO_2 order, which are diminished further (zoomed in the inset) at lowered resistance near 353 K at the R_2-VO_2 orders at the major R-VO_2 phase. Small R-VO_2 resistance is merged in that of resistive M_2/R_1-VO_2 phases. An equivalent circuit in the inset in **Figure 5.6 (a)** displays a net resistance at a VO_2 film involves (i) a resistance R_o between the electrodes, (ii) a capacitance C_p, (iii) an inductance L at a resistance R_x and (iv) a resistance R_e outside the electrodes. In a working frame, we ignore R_e and take $R_x \sim R_o$ in the R_o dominates as follows. Thus, distinct inflections are marked at the $M_1 \rightarrow M_2/R_1/R_2$/R-$VO_2$ orders in the derivative $Z^* = \partial Z''/\partial Z'$ plots over Z′ in **Figure 5.6 (b)** at the respective temperatures. For example, at $T_c \sim 343$ K, a shallow dip at 1.2×10^2 Hz in the R_1-VO_2 order follows two maxima in the R_2/R-VO_2 orders at 10^3 and 10^4 Hz, respectively. At a higher 353 K, the R-VO_2 is shifted over higher frequencies in all the three VO_2 phases (zoomed in the inset) are rather pushed apart at a frequency scale. The $R_2 \rightarrow$ R-VO_2 order (maxima) is gradually shifted over 10^4 Hz to 10^5 Hz as the temperature is raised 303 K to 353 K in a kinetically regulated surface order. It is an opposite trend to the T_{ce} is blue shifted in the s-SNOM images at THz frequencies [21, 22]. Further, coupled ‘e-p’ states hold a board band $M_1 \rightarrow M_2$-VO_2 over the frequencies.

At 363 K - 473 K, well beyond the T_c point, an overall different pattern of the Nyquist plots is portrayed in **Figure 5.6 (c)** in the R_o is gradually decreased at deep metallic VO_2 states. A small semicircle (R_2-VO_2), which is closely placed (right) to the major semicircle (R-VO_2), is slowly vanished at raising the temperature, showing a rich R-VO_2 at ≥ 393 K at 10^2 Hz to 10^6 Hz frequencies.

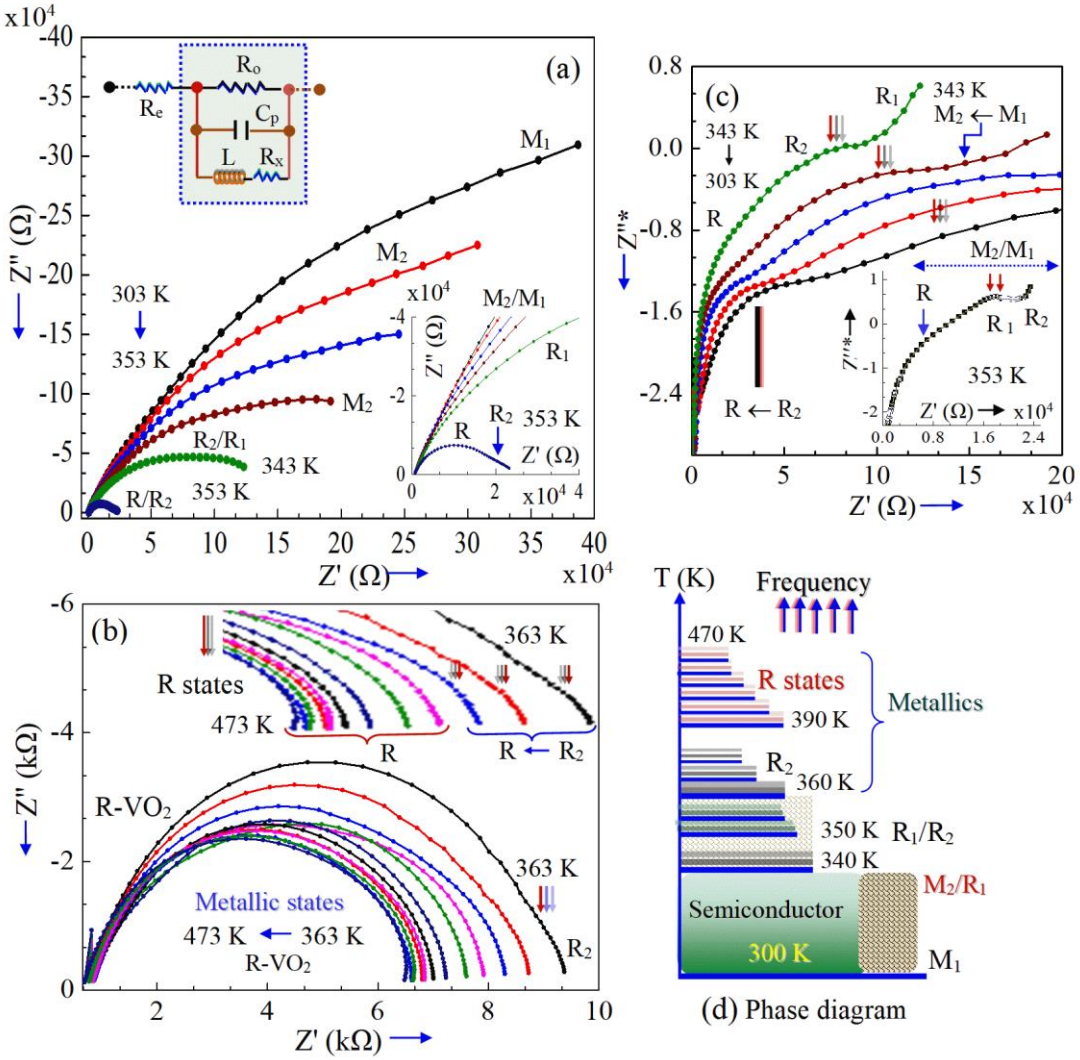

Figure 5.6 Nyquist plots at frequency (10^2 Hz to 10^6 Hz) induced charge order in a film VO_2@SiO_2-Si at (a) 303 K to 353 K and (b) 363 K to 473 K (taken at 10 K intervals), (c) with Z′′ derivatives (Z′′*) (a) plots over Z′ showing the itinerant transitions. The insets present (a) a LCR circuit at an inductance L (resistance R_x) and an external resistance R′, and a closer view Z′′-Z′ at (a, b) the intermediate VO_2 states. (d) A model phase diagram of itinerant VO_2 states over the temperatures/frequencies.

Thus, an average $Z = (Z'^2 + Z''^2)^{1/2} \cong 5.9$ kΩ shown for the R-VO_2 at 363 K is slowly declined up to 4.3 kΩ at 473 K at a thermal coefficient $(\alpha_R) \cong (\partial Z/\partial T)/Z_{av} \cong (-)$ 0.29 $\%K^{-1}$ at a mean $Z_{av} = 5.1$ kΩ value. It is as small as $\alpha_R = 0.37\ \%K^{-1}$ in gold, but negative in a deep charge order (a quasiparticle nature). Parts of the Nyquist plots zoomed in the

inset in **Figure 5.6 (c)** elucidate they are well dispersed at induced metallicity over the frequencies. A model in **Figure 5.6 (d)** projects a way the $M_1 \rightarrow M_2/R_1/R_2/R\text{-}VO_2$ states can order and displace one after others at a temperature (or the frequency) scale. The basic phonon levels and harmonics (marked at hatched areas) mediate the charge order at the correlated VO_2 states. Progressively enriched 'e-e' interactions at gradually decoupled 'e-p' regulate the $R_1 \rightarrow R_2/R\text{-}VO_2$ metallic states.

Further, we estimated R_o, L and C_p (in a parallel combination of an equivalent circuit [38]) at a simulation of the impedance data measured at the thin VO_2 films, using the ZsimpWin software. A net R_n resistance, $R_n^{-1} \cong R_o^{-1} + X_\ell^{-1} - R_c^{-1}$, operates at X_ℓ and R_c the contributions from L and C_p, respectively. So obtained R_o, L and C_p values plot a nonlinear response in **Figure 5.7 (a, b, c)** over the temperatures, wherein both R_o and L are diminished abruptly with the C_p is enhanced abruptly at the $T_{ce} \sim 353$ K (marked at the vertical line). It is the first order T_{ce} what is it is well enhanced as soon as decouples from the $T_{cs} \sim 343$ K in a vital effect of the frequencies. At $T > T_{ce}$, the device, as a capacitor, stores charge marked in a hatched area in **Figure 5.7 (c)**, so to the R_n does not decline even at well-metallized $R\text{-}VO_2$ states. $C_p \sim 5.6$ nF estimated at $T_{ce} \sim 353$ K is doubled at $T \rightarrow 473$ K. A smaller $C_p = 0.25$ nF is reported at 293 K (at 1 MHz) for thin $HfO_2/VO_2/HfO_2$@n-Si films, which is merely enhanced by an order over 293 K to 373 K [41]. An enhanced dielectric permittivity of 36 at 293 K to as large as $6x10^4$ in this regime indorses a good capacitor [42, 43]. So, it backs up a negative α_R even at the deeply metallized $R\text{-}VO_2$ states. Thus, at $T \geq 363$ K, as portrayed at a zoomed scale in **Figure 5.7 (d)**, the emerging R_o follows a polynomial over T^{-1}, with small kinks at 415 K and 450 K, in a surface order.

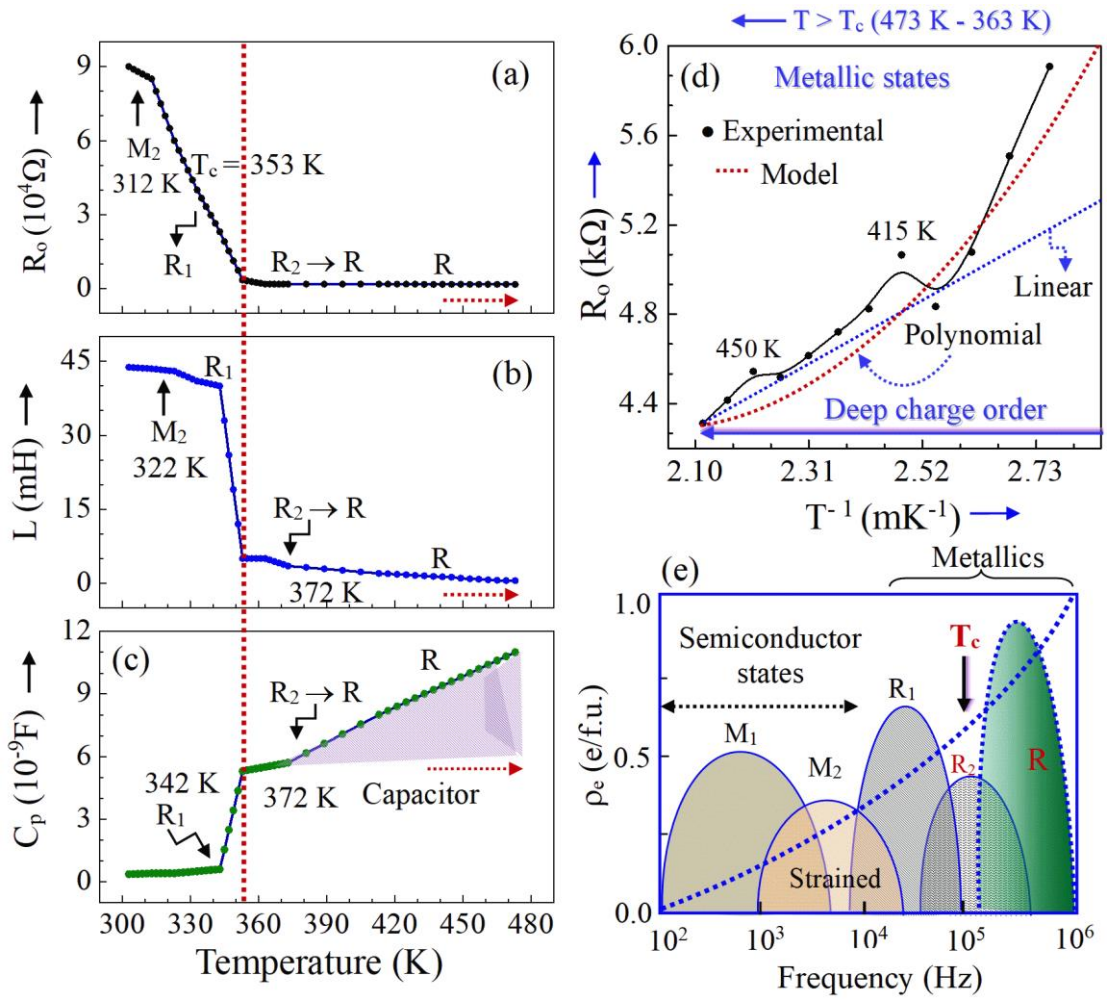

Figure 5.7 Thermal response of (a) R_o, (b) L and (c) C_p in an equivalent LCR circuit at a film VO_2@SiO_2-Si, showing the T_c ~ 353 K (vertical line). While the R_o and L are rapidly diminished, the C_p is rapidly enhanced at the T_c point, and arises up linearly at deep metallic R-VO_2 states. (d) A closer R_o view of it rises up gradually at a nonlinear α_R over T^{-1}, with weak inflections at 415 K and 450 K, and (e) a model $M_1 \rightarrow M_2/R_1/R_2$-R-$VO_2$ order at frequencies (RT).

It follows a polynomial,

$$<R_o> = R_m + \alpha_1 T^{-1} + \alpha_2 T^{-1} + \alpha_3 T^{-2} + \text{---}$$

$$\cong R_m + (\alpha_1 + \alpha_2)\, T^{-1} + \alpha_3 T^{-2}, \qquad (4)$$

which can be simplified in a parabolic route,

$$<R_o> \cong R_m + \alpha_3 T^{-2}, \qquad (5)$$

at a prominent effect of the 'electrostatic field' of the surface charges. Here, the coefficients α_1/α_2 describe the effects of the 'e-e' interactions and the surface VO_2 order, respectively, while that of α_3 arises at the electrostatic field at the surfaces. As usual, non-bridging O^{2-} at VO_2 NCs forms a negatively charged layer of an electrostatic field [26, 39]. Thus, arbitrary $\alpha_3 \sim 1.06 \times 10^8\ \Omega\text{-K}^2$ in Eq. (5) simulate the observed plot over 473 K to 363 K in **Figure 5.7 (d)** at $<R_o> = R_m \cong 4.3\ k\Omega$ at the deep metallized R-VO_2 states. Assuming $\alpha_3 \rightarrow 0$ in the absence of surface charges, Eq. (4) plots a straight line at $\alpha_1 + \alpha_2 \sim 1.37 \times 10^6\ \Omega\text{-K}$ in a deep surface R-VO_2 order. **Figure 5.7 (e)** projects a state-of-art of the $M_1 \rightarrow M_2/R_1/R_2/R\text{-}VO_2$ phases can order one after others at a thermal/frequency induced $3d^1\text{-}V^{4+}$ electrons, $\rho_e = 0$ to 1.0 e per formula VO_2 unit (f. u.), order near the E_F level (promoting the metallicity) over a frequency (or temperature) scale.

In thermodynamics, a lattice VO_2 can order in atoms and/or charges (or orbitals) $3d^1\text{-}V^{4+}$ in a way to optimize its net energy at a microscopic scale [25, 26]. At $\rho_e \leq 1.0$ e/f.u., the $3d^1$-orbitals polarize in a lattice rather than to interact so strongly with the surroundings in a VO_2 sample. Coupled 'e-p' mediate the orbitals (spins) swipe in a lattice up to a critical scale of its stability. Different ρ_e states in different VO_2 NCs in a sample order according to their average ρ_e states over a driving parameter. Thus, let us consider that an $M_1 \rightarrow M_2\text{-}VO_2$ lattice orders at ρ_e states in a domain, $T \leq T_1$, of 'e-p' states, as $T \rightarrow T_1$. A model DFT function [29, 43],

$$\rho_e(T) = \rho_e(0)\ \{1 - \exp(-\gamma_1 \Delta T_1^{\eta})\}, \tag{6}$$

assuming $\partial\rho_e(T)/\partial T \cong \partial N_e(T)/\partial T \cong \partial\sigma_o(T)/\partial T$, simulates a thermal-induced ρ_e (atoms N_e) orders towards conducting $\sigma_o = R_o^{-1}$ state in an $M_2\text{-}VO_2$ phase,

$$\frac{\partial\rho_e(T)}{\partial T} = T_{m2}(M_2) + \Omega_1\rho_e(T_{m2})\gamma_1\eta\{1-\Phi_1\}\Delta T_{m2}^{\eta-1}. \tag{7}$$

Let us assume that a model lattice begins to order at an inset, $T_{m2}(M_2) \sim 320$ K, and spans over $\Delta T_{m2} \sim 30$ K, as observed in the $M_1 \rightarrow M_2$-VO_2 band in **Figure 5.6 (a)**, with $\Phi_1 = 1- \exp(-\gamma_1 \Delta T_1^{\eta})$. As compiled in **Figure 5.8 (a)**, a peak arises at a critical temperature, $T_{m2}(M_2) = \{(\eta-1)/\gamma_1\eta\}^{1/\eta}$, as derived at a boundary condition $\partial^2\rho_e/\partial^2 T = 0$ in Eq. (7). At an arbitrary damping $\gamma_1 = 2.5 \times 10^{-3}$ $K^{-\eta}$, used to model a presumed $M_1 \rightarrow M_2$-VO_2 order, a resulting signal shifts over 320 K to 350 K, as the power 'η' is declined in small 0.5 steps, up to 1.5, assuming a partial $\rho_e(M_2) \cong 0.3$ e/f.u at the signal begins, where $\Omega_1 \cong 1$ K is taken as a scaling factor. It regularly shifts and spans over higher temperatures, as $\eta \rightarrow 1.5$, at the loss of its intensity until the next R_1-VO_2 phase ultimately starts to order at higher ρ_e values. As given in the inset in **Figure 5.8 (a)**, a band shifts over 325 K to 331 K of its peak value at γ_1 is declined 3×10^{-3} $K^{-\eta}$ to 0.5×10^{-3} $K^{-\eta}$ at $\eta = 5.0$ that gives a maximum peak intensity. Thus, both η and γ_1 are highly effective in tuning the final band so that it regularly spans, loses its intensity, and shifts at larger temperatures. They describe an integrated lattice-charge dynamics of unified VO_2 NCs embedding in the films.

Analogously, a function $\Phi_2 = 1-\exp(-\gamma_2 \Delta T_R^{\vartheta})$ can be extended to model a thermal-induced R-VO_2 order at rich metallic $\rho_e(T_R)$ states. It gives a derivative,

$$\frac{\partial \rho_e(T)}{\partial T} = T_R(R) + \Omega_2 \rho_e(T_R) \gamma_2 \vartheta \{1-\Phi_2\} \Delta T_R^{\vartheta-1} \qquad (8)$$

which presents a phase R-VO_2 order that begins in a band $\Delta T_R \cong 30$ K at $T_R(R) \cong 335$ K and spans over a presumed surface order of the atoms. A sharp peak thus set up at $T_R(R) = \{(\vartheta-1)/\gamma_2\vartheta\}^{1/\vartheta} \cong 338$ K at $\vartheta = 5.0$ and $\gamma_2 = 3.0 \times 10^{-3}$ $K^{-\vartheta}$ is regularly modulated up to

as much as 353 K in **Figure 5.8 (b)**, but a diffuse band at the loss of its intensity, as 'ϑ' is swiped up to 2.0 at the γ_2 is fixed, assuming $\rho_e(R) \sim 1.0$ e/f.u. and $\Omega_2 \cong 1.0$ K.

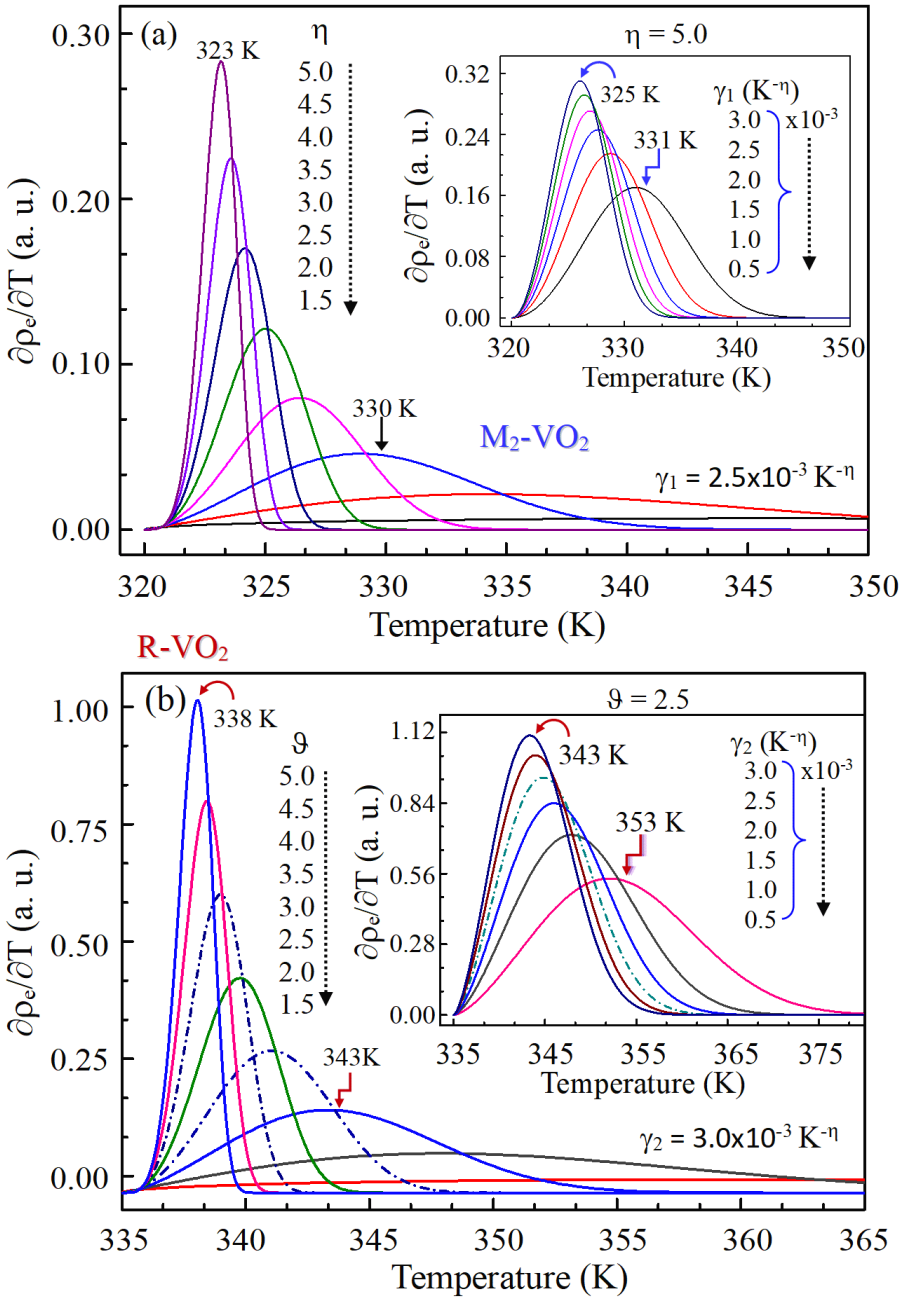

Figure 5.8 A model distribution of a thermal-induced charge-density ρ_e orders as a function temperature in a correlated (a) $M_1 \rightarrow M_2$-VO_2 and (b) $R_2 \rightarrow$ R-VO_2 phase order. The powers η and ϑ are regularly declined 5.0 to 1.5 at (a) $\gamma_1 = 2.5\text{x}10^{-3}$ $K^{-\eta}$ and (b) $\gamma_2 = 2.5\text{x}10^{-3}$ $K^{-\eta}$ in the model relations (7) and (8), respectively. The plots made at varied modulators γ_1/γ_2 over $0.5\text{x}10^{-3}$ $K^{-\eta}$ to $3.0\text{x}10^{-3}$ $K^{-\eta}$ at $\eta = 5.0$ and $\vartheta = 2.5$ are added in the insets, respectively.

A sharper band is tuned from 343 K to 353 K (peak values) in similar plots in the inset in **Figure 5.8 (b)** at $3x10^{-3}\,K^{-\vartheta} \leq \gamma_2 \leq 0.5x10^{-3}\,K^{-\vartheta}$, with $\vartheta = 2.5$, at no change in the other parameters. The intermediate VO_2 states share similar microscopic bands ordered one over others as given in a model in **Figure 5.7 (e)**. The results anticipate the effects of the phase/charge orders shown in the s-SNOM images and other properties. Decoupled $3d^1$-V^{4+} electrons (orbitals) carry over a deep charge order (increasing σ_o) at the metallic R-VO_2 states. Similar signals can be formulated at frequency, electric fields, or other driving operators.

5.3 Conclusion

The nanostructured VO_2 of thin films (thickness $t \leq 100$ nm) has wide applications of integrated electronics, optical memory, neuromorphic computing, and many other devices. It executes a reversible transition of its structure and SC to metallic states at a T_c ~ 343 K. That is utilized to exchange energy in such devices. Extensive studies are made on harvesting the T_c and emerging properties useful for the applications. In fact, a series of $M_1 \rightarrow M_2/R_1/R_2$-R-$VO_2$ phases mediate the exotic features that are studied systematically in this work in terms of their impedance resistance R_o regulated at frequencies. The individual phases are shown to order at correlated charge order (metallizing) without a phase separation at VO_2 NCs embedding in the films, as heated 303 K to 473 K at10^2 Hz to 10^6 Hz frequencies. The frequency deprives coupled electron-phonon 'e-p' states and induce $3d^1$-V^{4+} electrons (coupled to the holes 'h^+' in the VB) filling up (metallizing) the bandgap across the Fermi surface. Thus, even near RT, a surface order $M_1 \rightarrow M_2/R_1/R_2$/R-$VO_2$ incurs over 10^2 to 10^6 Hz frequencies, respectively. The R_1/R_2-VO_2 (semi-metallics) extend well beyond T_c at the charge order prolongs at the metallic R-VO_2 states, well up to 473 K (or even more), over a frequency scale. All

the five distinct VO_2 phases are well mapped in MIR field s-SNOM images of the VO_2 films. The results anticipate a kinetic response of the T_c point at decoupled $3d^1$ electrons (orbitals) so that it is regularly shifted from 343 K at THz (5-10 meV) to 353 K at MIR (125 meV) fields used in the s-SNOM imaging at a nanoscale. Consistently, it is blue-shifted in the frequency modulated R_o (up to 10^5 times) as well at the charge order. The correlated phase-charge order delineates the strategy of exotic properties of thin VO_2 film technologies.

REFRENCES

[1] Z. He, Z. Qi, B. Yang, P. Lu, J. Shen, N. R. Dilley, X. Zhang, and H Wang, "Controllable Phase Transition Properties in VO_2 Films via Metal-Ion Intercalation," *Nano Letters*, **23** (2023) 1119−1127.

[2] M. Liu, X. Li, L. Li, L. Li, S. Zhao, K. Lu, K. Chen, J. Zhu, T. Zhou, C. Hu, Z. Lin, C. Xu, B. Zhao, G. Zhang, G. Pei, and C. Zou, "Continuous Photothermal and Radiative Cooling Energy Harvesting by VO_2 Smart Coatings with Switchable Broadband Infrared Emission," *ACS Nano*, **17** (2023) 9501−9509.

[3] Y. Sharma, J. Balachandran, C. Sohn, J. T. Krogel, P. Ganesh, L. Collins, A. V. Ievlev, Q. Li, X. Gao, N. Balke, O. S. Ovchinnikova, S. V. Kalinin, O. Heinonen, and H. N. Lee, "Nanoscale Control of Oxygen Defects and Metal–Insulator Transition in Epitaxial Vanadium Dioxides," *ACS Nano*, **12** (2018) 7159–7166.

[4] E. Strelcov, A. Tselev, I. Ivanov, J. D. Budai, J. Zhang, J. Z. Tischler, I. Kravchenko, S. V. Kalinin, and A. Kolmakov, "Doping-Based Stabilization of the M_2 Phase in Free-Standing VO_2 Nanostructures at Room Temperature," *Nano Letters*, **12** (2012) 6198−6205.

[5] S. Lee, C. Cheng, H. Guo, K. Hippalgaonkar, K. Wang, J. Suh, K. Liu, and J. Wu, "Axially Engineered Metal−Insulator Phase Transition by Graded Doping VO_2 Nanowires," *Journal of the American Chemical Society*, **135** (2013) 4850−4855.

[6] J. Cao, Y. Gu, W. Fan, L. Q. Chen, D. F. Ogletree, K. Chen, N. Tamura, M. Kunz, C. Barrett, J. Seidel, and J. Wu, "Extended Mapping and Exploration of the Vanadium Dioxide Stress-Temperature Phase Diagram," *Nano Letters*, **10** (2010) 2667−2673.

[7] M. K. Liu, M. Wagner, E. Abreu, S. Kittiwatanakul, A. McLeod, Z. Fei, M. Goldflam, S. Dai, M. M. Fogler, J. Lu, S. A. Wolf, R. D. Averitt, and D. N. Basov, "Anisotropic Electronic State via Spontaneous Phase Separation in Strained Vanadium Dioxide Films" *Physical Review Letters*, **111** (2013) 096602 (5).

[8] D. Passarello, S. G. Altendorf, J. Jeong, C. Rettner, N. Arellano, T. Topuria, M. G. Samant, and S. S. P. Parkin, "Evidence for Ionic Liquid Gate-Induced Metallization of Vanadium Dioxide Bars over Micron Length Scales" *Nano Letters*, **17** (2017) 2796−2801.

[9] S. Lee, X. G. Sun, A. A. Lubimtsev, X. Gao, P. Ganesh, T. Z. Ward, G. Eres, M. F. Chisholm, S. Dai, and H. N. Lee, "Persistent Electrochemical Performance in Epitaxial VO_2(B)" *Nano Letters*, **17** (2017), 2229−2233.

[10] T. Wang, D. Torres, F. E. Fernández, A. J. Green, C. Wang, and N. Sepúlveda, "Increasing Efficiency, Speed, and Responsivity of Vanadium Dioxide Based Photothermally Driven Actuators Using Single-Wall Carbon Nanotube Thin-Films" *ACS Nano*, **9** (2015) 4371−4378.

[11] W. K. Hong, J. B. Park, J. Yoon, B. J. Kim, J. I. Sohn, Y. B. Lee, T. S. Bae, S. J. Chang, Y. S. Huh, B. Son, E. A. Stach, T. Lee, and M. E. Welland, "Hydrogen-Induced

Morphotropic Phase Transformation of Single-Crystalline Vanadium Dioxide Nanobeams," *Nano Letters*, **13** (2013) 1822−1828.

[12] J. Lin, H. Ji, M. W. Swift, W. J. Hardy, Z. Peng, X. Fan, A. H. Nevidomskyy, J. M. Tour,and D. Natelson, "Hydrogen Diffusion and Stabilization in Single-Crystal VO_2 Micro/Nanobeams by Direct Atomic Hydrogenation," *Nano Letters*, **14** (2014) 5445–5451.

[13] M. Nakano, K. Shibuya, D. Okuyama, T. Hatano, S. Ono, M. Kawasaki, Y. Iwasa, and Y. Tokura, "Collective Bulk Carrier Delocalization Driven by Electrostatic Surface Charge Accumulation," *Nature*, **487** (2012) 459–462.

[14] J. Jeong, N. Aetukuri, T. Graf, T. D. Schladt, M. G. Samant, and S. S. P. Parkin, "Suppression of Metal-Insulator Transition in VO_2 by Electric Field–Induced Oxygen Vacancy Formation," *Science*, **339** (2013) 1402–1405.

[15] S. Lee, T. L. Meyer, C. Sohn, D. Lee, J. Nichols, D Lee, S. S. A. Seo, J. W. Freeland, T. W. Noh, and H. N. Lee, "Electronic Structure and the Insulating Gap in Epitaxial VO_2 Polymorphs," *APL Materials*, **3** (2015) 126109 (7).

[16] P. K. Ojha, R. Sharma, S. K. Mishra, and S. Ram, "Charge Ordering at a Dielectric Gate in Itinerant Metallic States with Low-Field Memristor Properties in VO_2 Thin Films," *Surfaces and Interfaces*, **42** (2023) 103445 (14).

[17] H. Shim, and G. Lee, "True First-Order Surface Phase Transition without Nanoscale Phase Separation," *ACS Nano*, **17** (2023) 11764−11770.

[18] L. Li, H. Chen, Y. Shi, and D. Xing, "Human-Body-Temperature Triggerable Phase Transition of W‑VO_2@PEG Nanoprobes with Strong and Switchable NIR-II Absorption for Deep and Contrast-Enhanced Photoacoustic Imaging," *ACS Nano*, **16** (2022) 2066–2076.

[19] A. Cvitkovic, N. Ocelic, and R. Hillenbrand, "Material-Specific Infrared Recognition of Single Sub-10 nm Particles by Substrate-Enhanced Scattering-Type Near-Field Microscopy," *Nano Letters*, **7** (2007) 3177−3181.

[20] C. McGahan, S. Gamage, J. Liang, B. Cross, R. E. Marvel, R. F. Haglund, and Y. Abate, "Geometric Constraints on Phase Coexistence in Vanadium Dioxide Single Crystals," *Nanotechnology*, **28** (2017) 085701 (9).

[21] H. T. Stinson, A. Sternbach, O. Najera, R. Jing, A. S. Mcleod, T. V. Slusar, A. Mueller, L. L. Anderegg, H. T. Kim, M. Rozenberg, and D. N. Basov, "Imaging the Nanoscale Phase Separation in Vanadium Dioxide Thin Films at Terahertz Frequencies" *Nature Communication*, **9** (2018) 3604 (9).

[22] C. Hu, L. Li, X. Wen, Y. Chen, B. Li, H. Ren, S. Zhao, and C. Zou, "Manipulating the Anisotropic Phase Separation in Strained VO_2 Epitaxial Films by Nanoscale Ion-Implantation," *Applied Physics Letters*, **119** (2021) 121101 (6).

[23] X-Ray Powder Diffraction JCPDS Files, (a) 01-082-661; VO_2 Monoclinic, (b) 01-079-1655; VO_2 Rutile, and (c) 01-083-2469; SiO_2-P_{3121} Hexagonal, Joint Committee on Powder Diffraction Standard International Centre for Diffraction Data, Swarthmore, PA, USA, **2019**.

[24] G. K. Williamson, and W. H. Hall, "X-Ray Line Broadening from Filed Aluminium and Wolfram," *Acta Metallurgica*, **1** (1953) 22–31.

[25] S. Ram, "Self-Confined Dimension of Thermodynamic Stability in Co-Nanoparticles in FCC and BCC Allotropes with a Thin Amorphous Al_2O_3 Surface Layer," *Acta Materialia*, **49** (2001) 2297–2307.

[26] S. Ram, "Synthesis and Structural and Optical Properties of Metastable ZrO_2 Nanoparticles with Intergranular Cr^{3+}/Cr^{4+} Doping and Grain Surface Modification," *Journal of Materials Science*, **38** (2003) 643–655.

[27] S. Guan, A. Rougier, M. R. Suchomel, N. Penin, K. Bodiang, and M. Gaudon, "Geometric Considerations of the Monoclinic-Rutile Structural Transition in VO_2," *Dalton Transactions*, **48** (2019) 9260–9265.

[28] R. M. Wentzcovitch, W. W. Schulz, and P. B. Allen, "VO_2: Peierls or Mott-Hubbard? A View from Band Theory," *Physical Review Letters*, **72** (1994) 3389–3392.

[29] S. K. Sharma, D. S. Saini, D. Pradhan, and S. Ram, "Grafted Magnet C-$Mn_{0.5}Bi_{0.5}$ with a Cohesive C-sp^2 Spin Layer and Its Impacts on the Exchange-Coupled Magnetic Properties," *Journal of Alloys and Compounds*, **973** (2024) 172770 (18).

[30] B. Hong, K. Hu, Z. Tao, J. Zhao, N. Pan, X. Wang, M. Lu, Y. Yang, Z. Luo, and C. Gao, "Polymorph Separation Induced by Angle Distortion and Electron Delocalization Effect *via* Orbital Modification in VO_2 Epitaxial Thin Films," *Physical Review B*, **95** (2017) 075433 (8).

[31] V. Balédent, T. T. F. Cerqueira, R. Sarmiento-Pérez, A. Shukla, C. Bellin, M. Marsi, J. P. Itié, M. Gatti, M. A. L. Marques, S. Botti, and J. P. Rueff, "High-Pressure Phases of VO_2 from the Combination of Raman Scattering and *ab initio* Structural Search," *Physical Review B*, **97** (2018) 024107 (7).

[32] Y. Liu, X. Qiu, S. Soni, and R. C. Chiechi, "Charge Transport through Molecular Ensembles: Recent Progress in Molecular Electronics," *Chemical Physics Reviews*, **2** (2022) 021303 (40).

[33] A. Sohn, H. Kim, D. W. Kim, C. Ko, S. Ramanathan, J. Park, G. Seo, B. J. Kim, J. H. Shin, and H. T. Kim, "Evolution of Local Work Function in Epitaxial VO_2 Thin Films Spanning the Metal-Insulator Transition," *Applied Physics Letters*, **101** (2012) 191605 (3).

[34] W. R. Mondal, E. Evlyukhin, S. A. Howard, G. J. Paez, H. Paik, D. G. Schlom, L. F. J. Piper, and W. C. Lee, "Role of V-V Dimers on Structural, Electronic, Magnetic, and Vibrational Properties of VO_2 by First-Principles Simulations and Raman Spectroscopic Analysis," *Physical Review B*, **103** (2021) 214107 (13).

[35] S. S. Majid, D. K. Shukla, F. Rahman, S. Khan, K. Gautam, A. Ahad, S. Francoual, R. J. Choudhary, V. G. Sathe, and J. Strempfer, "Insulator-Metal Transitions in the *T* Phase Cr-Doped and M_1 Phase Undoped VO_2 Thin Films," *Physical Review B*, **98** (2018) 075152 (9).

[36] M. Wagner, J. Planer, B. S. J. Heller, J. Langer, A. Limbeck, L. A. Boatner, H. P. Steinrück, J. Redinger, F. Maier, F. Mittendorfer, M. Schmid, and U. Diebold, "Oxygen-Rich Tetrahedral Surface Phase on High-Temperature Rutile VO_2 $(110)_T$ Single Crystals," *Physical Review Materials,* **5** (2021) 125001 (15).

[37] R. Basu, V. Srihari, M. Sardar, S. K. Srivastava, S. Bera, and S. Dhara, "Probing Phase Transition in VO_2 with the Novel Observation of Low-Frequency Collective Spin Excitation," *Scientific Report,* **10** (2020) 1977 (11).

[38] J. G. Ramírez, R. Schmidt, A. Sharoni, M. E. Gómez, I. K. Schuller, and E. J. Patińo, "Ultra-Thin Filaments Revealed by the Dielectric Response Across the Metal-Insulator Transition in VO_2," *Applied Physics Letters,* **102** (2013) 063110 (4).

[39] B. Tiwari, S. Ram, and P. Banerji, "Biogenic Synthesis of Tunable Core-Shell C-$CaIn_2O_4$, Interface Bonding, Conductive Network Channels, and Tailored Dielectric Properties," *ACS Sustainable Chemistry and Engineering,* **6** (2018) 16298–16307.

[40] S. Jangu, S. K. Sharma, and S. Ram, "A metastable Cr^{4+}-Compound $AlCrO_{3+\delta}$, $\delta \leq 0.5$, Grown at a Nanocolloid, and Its Ultraviolet Absorption, Phonon Bands, and Dielectric Properties," *Journal of Alloys and Compounds*, **927** (2022) 166865 (11).

[41] Z. Yang, C. Ko, V. Balakrishnan, G. Gopalakrishnan, S. Ramanathan, "Dielectric and Carrier Transport Properties of Vanadium Dioxide Thin Films Across the Phase Transition Utilizing Gated Capacitor Devices," *Physical Review B,* **82** (2010) 205101 (8).

[42] P. K. Ojha, R. Sharma, V. G. Sathe, S. Ram, and S. K. Mishra, "Dynamics of Phonons, Charge-Regulated Itinerant VO_2 States, and their Impacts on the Memristor Properties of Thin VO_2 Films," *Surfaces and interfaces,* **46** (2024) 104029 (19).

[43] S. Misra, T. Karan, and S. Ram, "Dynamics of Surface Spins in Small Core-Shell Magnets of $Li_{0.35}Zn_{0.30}Fe_{2.35}O_4$ Bonds over a Carbon Surface and Tailored Magnetic Properties," *Journal of Physical Chemistry C,* **119** (2015) 23184–23195.